PAPER

Check for updates

Long-range magnetic interaction of native defects in transition metal dichalcogenides†

Prashant Vijay Gaikwad, [ID] [abd] T. Thuy Hoang, [ID] [ac] Sungjin Park[ab] and Junhyeok Bang [ID] *[ab]

Recent experiments have revealed weak ferromagnetism in pristine transition metal dichalcogenides (TMDs), although the underlying mechanism remains unclear. In this work, we investigate the possibility of native defects inducing ferromagnetism in TMDs, specifically WS_2 and MoS_2. Among the various native defects, we have identified that cation antisites exhibit localized magnetic moments of $2\mu_B$. These localized moments tend toward ferromagnetic ordering *via* magnetic interactions facilitated by local spin density oscillations. While the strength of the magnetic interactions is comparable to that of magnetic dopants in TMD, they are significantly weakened when the distance between the two antisites exceeds 9 Å. Therefore, our results suggest that native-defect-induced ferromagnetism in TMD is feasible only in heavily defective TMD samples.

1. Introduction

The discovery of two-dimensional (2D) magnetic materials such as CrI_3 and $CrGeTe_3$ was a great scientific and practical advance.[1,2] In the scientific aspect, the existence of the long-range magnetic order in the 2D systems has been a fundamental question, as the Mermin–Wagner theorem suggested that the 2D long-range orders are destroyed by the thermal fluctuations.[3] Currently, 2D magnetism is understood based on the effect of the magnetic anisotropy by transferring the 2D system from the Heisenberg model to the Ising model.[2] In the practical aspect, the realization of the 2D magnetic systems could lead to new 2D-based magnetic applications.[4–9] Several 2D materials with exceptional electric and optical properties have been found over the past decades and are considered to be a new family for novel device applications.[10–13] However, magnetism has been one property missing from 2D materials. The emergence of 2D magnets is likely to open new directions in 2D materials.

Among the 2D materials, graphene and transition metal dichalcogenides (TMDs) have been intensively studied due to their exceptional properties. Although they are non-magnetic in their pristine forms, many studies have been performed to introduce magnetism in them by doping with transition metals such as Mn, V, Cr, Fe, CO, and P.[14–20] In TMDs, the long-range ferromagnetic interaction can be established by super-exchange interaction among highly localized d-states of the transition metals by antiferromagnetically coupled delocalized p-states of chalcogenides. More interestingly, ferromagnetism has been experimentally observed in graphene without any intentional doping.[21–25] Many theoretical works have studied this graphene ferromagnetism, and it is now understood to be based on the pseudo-spin-mediated long-range ferromagnetic coupling between local magnetic moments generated by native defects or hydrogen absorption.[26–28]

Recent experiments have also observed a weak but room-temperature ferromagnetism in pristine (but possibly defective) TMDs such as WS_2 and MoS_2.[29–33] Because TMDs are semiconductors without the metallic pseudo-spin state that exists in graphene, the mechanism of the ferromagnetism of TMDs could be different from that in graphene. To explain the intrinsic ferromagnetism, several theoretical and experimental studies have been performed. Huo *et al.* proposed edge-state-induced ferromagnetism in WS_2.[29] Other groups have suggested that local metallic 1T phases inside the host 2H TMD can be ferromagnetically coupled and lead to ferromagnetism.[32,34]

As another possible mechanism, defects could also lead to ferromagnetism in TMDs, like in graphene. Native defects such as vacancies and interstitials are inevitably generated in the growth processes and can significantly affect the properties of TMDs.[35,36] It is known that defects in TMDs could have local magnetic moments,[35,37] and a previous work suggested the possibility of magnetically-active-defect-induced ferromagnetism.[30] However, the detailed mechanism of defect-induced ferromagnetism, especially long-range magnetic coupling between the magnetic defects, has not been studied yet.

[a]*Department of Physics, Chungbuk National University, Cheongju 28644, Republic of Korea. E-mail: jbang@cbnu.ac.kr*

[b]*Research Institute for Nanoscale Science and Technology, Cheongju 28644, Republic of Korea*

[c]*Basic Science Research Institute, Chungbuk National University, Cheongju 28644, Republic of Korea*

[d]*Department of Physics, Savitribai Phule Pune University, Pune-411007, India*

In this work, we have investigated the effects of native defects on the magnetic properties of TMDs such as WS_2 and MoS_2. First, we have examined isolated defects such as S vacancies (V_S), transition metal anti-sites (M_S, M = W or Mo), transition metal interstitials (M_i), and M_S and V_S complex defects (M_S–V_S), which have localized d-orbitals, and thus could have a localized magnetic moment. While V_S and M_i have no magnetic moment, M_S and M_S–V_S exhibit localized magnetic moments of $2\mu_B$. Second, we have studied the long-range magnetic interaction between M_S defects with respect to their relative positions. The magnetic interaction is mediated by the local spin density oscillation, and it shows that ferromagnetic couplings are favorable for most of the relative positions. However, the magnetic interaction varies with the relative position and is significantly reduced over the fourth-nearest neighboring site. Our results suggest that defect-induced ferromagnetism can be generated in heavily defective TMDs.

2. Methodology

The optimized atomic structures and relevant total energies were calculated based on spin-polarized density functional theory (DFT),[38,39] as implemented in the Vienna *ab initio* simulation package (VASP).[40–43] The plane augmented wave method was used to represent the ion cores,[44] and the generalized gradient approximation formulated by Perdew, Burke, and Ernzerhof was used for the exchange–correlation functional.[45,46] The wave-functions were expanded in a plane wave basis set up to a cut-off energy of 500 eV. To model the isolated defects and the magnetic coupling between two defects, we employed a periodic 7×7 supercell with a 15 Å vacuum region along the z-direction, which is sufficiently large to avoid artificial interaction between periodic images. For Brillouin-zone integration, a Γ-centered $3 \times 3 \times 1$ k-point mesh was used for ionic relaxation, and a denser $6 \times 6 \times 1$ k-point mesh was used for precise electronic structure calculations. Atomic structures were fully relaxed until the residual forces were less than 0.02 eV Å^{-1}. The spin–orbit coupling (SOC) was incorporated using an approximation of relativistic effects by a scalar relativistic Hamiltonian with SOC in a perturbation treatment.[47] However, the inclusion of SOC was found to have a minor effect on the energy of the magnetic coupling.

The formation energy $F_E(D)$ of a defect D was calculated as

$$F_E(D) = E(D) - E(Pure) - \sum_i \Delta n_i \mu_i$$

where $E(D)$ and $E(Pure)$ are the total energies of the defective and pure systems, respectively, and Δn_i and μ_i are the number change and the chemical potential of the i-th element, which are added ($\Delta n_i > 0$) or removed ($\Delta n_i < 0$). The chemical potentials used were the atomic total energies of the BCC phase for W and Mo metals and the orthorhombic phase for S.

3. Results and discussion

3.1. Localized magnetic moments in native defects

We first considered native defects in WS_2 that could generate a local magnetic moment. Among the various native defects, we focused on V_S, W_S, and W_i defects as shown in Fig. 1(a)–(c), respectively, because they have unpaired d-orbitals of W atoms, so they are likely to have a localized magnetic moment. This is not the case for the other isolated native defects such as W vacancies, S interstitials, and S anti-sites. All the defects we considered are likely to be formed in W-rich (or S-poor) growth conditions. In this regard, we assume W-rich WS_2 samples in this work.

Anion vacancies, *i.e.*, V_S in this case, have been widely observed in TMDs.[35,36,48] Our calculations also showed that V_S has the lowest formation energy, as shown in Table 1. However, V_S has no local magnetic moments, despite the existence of the non-bonding d-orbitals of the three neighboring W atoms [see Fig. 1(a)]. This is because of the inward relaxation of the three W atoms and the formation of the fully occupied bonding levels of the non-bonding d-orbitals, leaving the fully unoccupied d-levels in the gap. In pristine WS_2, the distance between two W atoms (D_{W-W}) is 3.18 Å. However, near the V_S defect, as shown in Fig. 1(a), D_{W-W} is reduced by 0.14 Å. This relaxation leads to the formation of a bonding level inside the valence band, effectively quenching the local magnetic moment.

In the W-rich growth conditions, the sufficient W adatoms are likely to encounter the abundant V_S sites on WS_2, and the V_S sites can be filled by the W atoms, forming cation anti-site defects W_S, as shown in Fig. 1(b). The inclusion of a W atom at the V_S site restores the D_{W-W} (3.12 Å) near the W_S defect [see Fig. 1(b)] to a value close to that of the pristine structure. Additionally, no significant changes were observed in other bonds, such as the W–S bonds. Our calculations showed that the W_S defect exhibits a local magnetic moment of $2\mu_B$, which is in good agreement with previous results.[49] Due to the different atomic environment of the W_S atom compared with that of the host W atoms, it shows different level splitting of the W_S d-orbitals. As shown in Fig. 2(a), the three d_{XY}, $d_{X^2-Y^2}$, and d_{Z^2} levels appear around the band gap, while the other two d_{XZ} and d_{YZ} levels are located below the valence band maximum (VBM). For the majority spin state, the d_{XY} and $d_{X^2-Y^2}$ levels are doubly degenerate at 0.91 eV, and the single d_{Z^2} level is located at 1.16 eV with respect to the VBM, as shown in Fig. 2(a). Note that the minority spin d_{XY}, $d_{X^2-Y^2}$, and d_{Z^2} levels are located near the conduction band minimum (CBM), showing large spin split-ting. W_S has effectively six valence electrons in the d-orbitals: four originate from the valence electrons of W_S and two origi-nate from the three neighboring W atoms. Among them, the four are filled into the d_{XZ} and d_{YZ} levels below VBM, and the doubly degenerate d_{XY} and $d_{X^2-Y^2}$ levels in the gap are occupied by the remaining two electrons. Therefore, this partial electron occupation of localized d-levels induces the large spin splitting by the exchange interaction,[14] and W_S can have a magnetic moment of $2\mu_B$.

The inset in Fig. 2(a) shows the spatial distribution of the spin density of W_S. The majority spin is highly localized near the W_S atom, resulting in an atomic magnetic moment $1.51\mu_B$. For the three nearest neighboring W atoms, however, the minority spin is distributed with an atomic magnetic moment of $-0.09\mu_B$ per each W atom. For the three next nearest neighboring W atoms, the majority spin is again distributed with a smaller
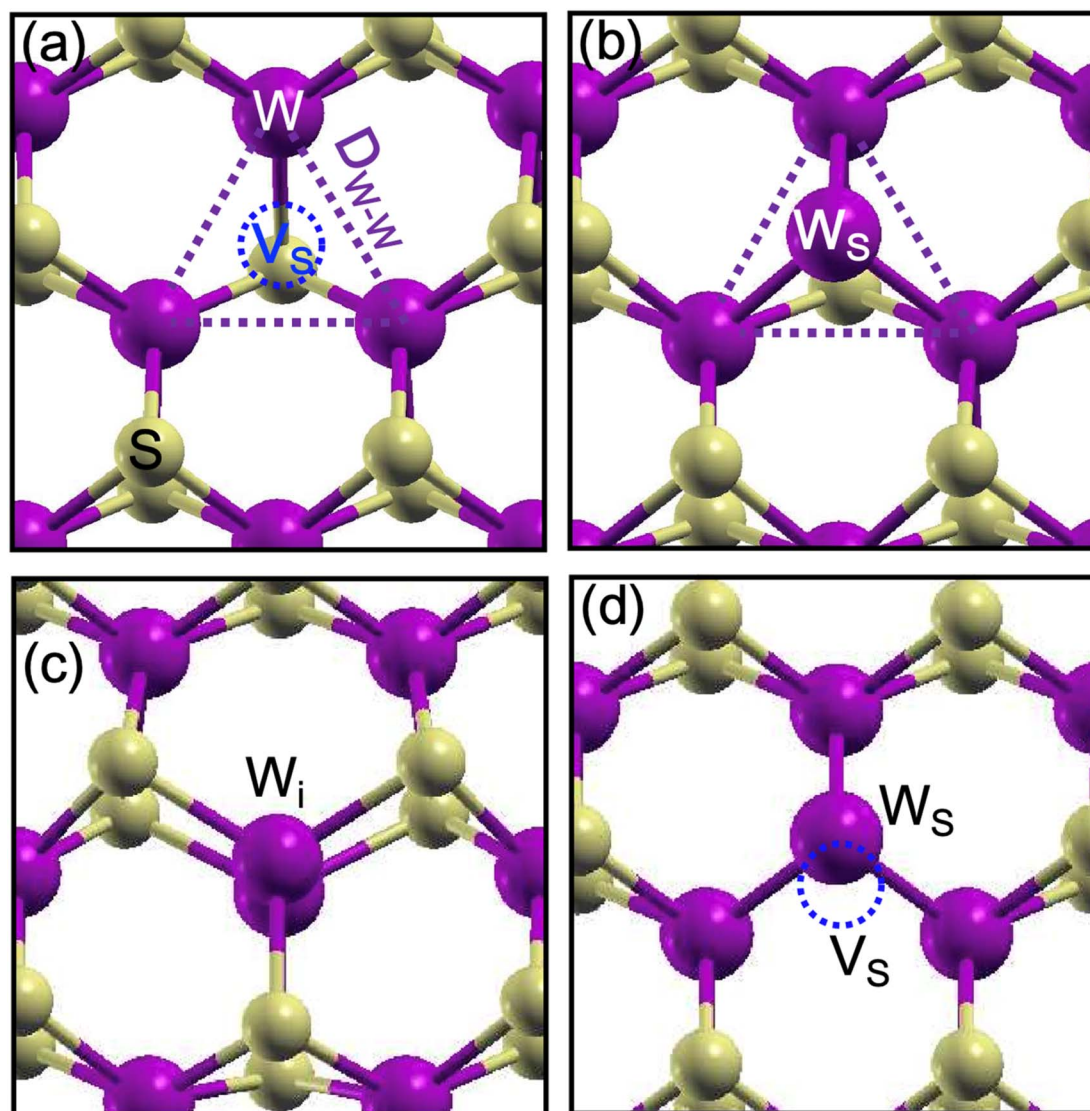
Fig. 1 Atomic structures of (a) S vacancy (V_S), (b) W antisite (W_S), (c) W interstitial (W_i), and (d) W_S–V_S complex defects in WS_2. In (a) and (d), vacancy sites are denoted by dotted blue circles. In (a) and (b), the neighboring W atoms near the defect are denoted by dotted violet lines. The W and S atoms are represented by magenta and yellow balls, respectively.

Table 1 Defect formation energies E_F in the cation- or anion-rich conditions, and the localized magnetic moments (m) of the various defects such as S vacancies (V_S), cation interstitials (M_i), cation antisites (M_S), and cation antisite and S vacancy complex (M_S–V_S) in WS_2 and MoS_2. M stands for W in WS_2 and Mo in MoS_2

	WS_2			MoS_2		
	E_F (eV)			E_F (eV)		
	W-rich	S-rich	m (μ_B)	Mo-rich	S-rich	m (μ_B)
V_S	1.56	2.79	0.0	1.33	2.63	0.0
M_i	5.30	7.77	0.0	3.86	6.47	0.0
M_S	5.45	9.14	2.0	3.86	7.78	2.0
M_S-V_S	6.74	11.66	2.0	5.14	10.36	2.0

local magnetic moment $0.09\mu_B$ per each W atom. The spin density oscillation is caused by the super-exchange interaction through an S atom.[49] Note that the magnetic moment on S atoms is very small because of the absence of d-orbitals. This spin density oscillation is induced by the W_S defect. Similar spin density oscillations have been found in graphene due to defects, but the spin density is distributed in much longer range, leading to long-range magnetic coupling.[26]

Fig. 1(c) shows the atomic structure of W_i. The W adatom is stabilized on the host W site, forming a symmetrically separated two W dumbbell structure. The formation energy of W_i in the W-rich condition is similar to, but a bit smaller than that of W_S (see Table 1). However, due to the bonding between the two W atoms, similar to V_W, W_i also has no magnetic moment.

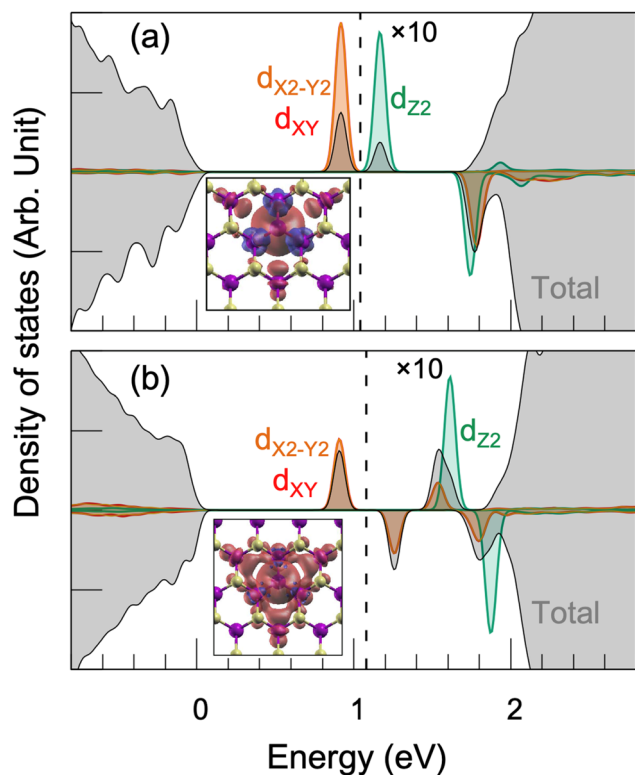We have summarized the formation energies and magnetic moments of the isolated defects discussed above in Table 1.

Fig. 2 Total and projected density of states (DOS) of (a) W_S and the (b) W_S–V_S complex. Upper (lower) panel is the majority (minority) spin DOS. Black lines and gray shaded regions are total DOS, and projected DOS are shown using the corresponding colors denoted in the figures. All the projected DOSs were scaled by a factor of 10 with respect to the total DOS. The valence band maximum was set to 0.0 eV, and the Fermi level is presented by the vertical dotted lines. Isosurfaces of the spin densities for W_S and the W_S–V_S complex are shown in the insets of (a) and (b), respectively.

While W_S has a localized magnetic moment, its formation energy is relatively high. Thus, under equilibrium growth conditions, the W_S concentration $[W_S]$ may be too low to lead to ferromagnetism in WS_2. However, under non-equilibrium growth conditions, $[W_S]$ can be significant due to a diffusion-limited kinetic process. In the process, W_S can be formed by the migration and clustering of V_S and W_i if the following two conditions are met: (i) attractive interaction between V_S and W_i, and (ii) activation of V_S or/and W_i diffusion.[50,51] For condition (i), our calculations show that the binding energy between V_S and W_i to form W_S is quite large (about 1.41 eV), implying a strong attractive interaction. For condition (ii), previous results showed that the diffusion energy barrier is about 0.6 eV for transition metal interstitials in TMD.[52] This is in good agreement with the fact that W_S as well as V_S are widely observed in experiments.[35,36] Hence, we will consider the effect of the anti-site defect W_S on the magnetic properties in TMD in the next section.

Until now, we have discussed isolated point defects in WS_2. In the non-equilibrium process that we considered above, large complex defects as well as W_S can be also formed by the kinetic processes of the isolated defects. The M_S–V_S complex [see Fig. 1(d)], which has been observed in experiments,[35] is an example. Regarding the two conditions above, (i) the binding energy between M_S and V_S is about 0.27 eV, and (ii) the V_S diffusion, for which the diffusion barrier is about 2.3 eV,[53] can be activated at the sample growth temperature of ~1000 K.[15,29] While the binding energy is small, and so the W_S–V_S concentration is expected to be low even in non-equilibrium conditions, the W_S–V_S complex can exist and could lead a localized magnetic moment in WS_2. As shown in Fig. 2(b), the doubly degenerate d_{XY} and $d_{X^2-Y^2}$ levels in the gap are occupied, and it has a local magnetic moment $2\mu_B$, similar to those of W_S. Previous works[54]
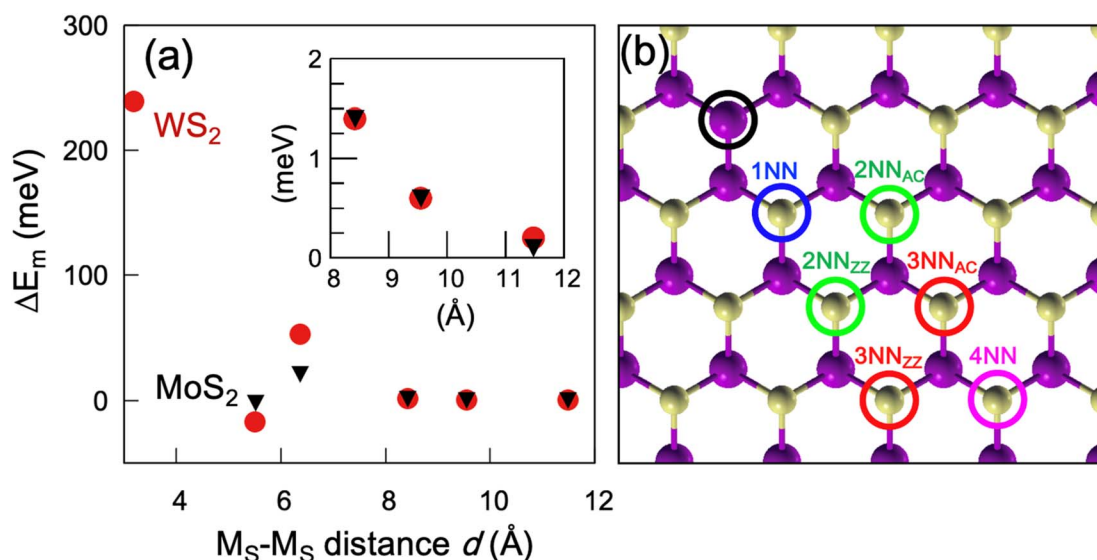

Fig. 3 Long-range magnetic interaction between two M_S defects (M = W for WS_2 and Mo for MoS_2). (a) Energy difference ΔE_m between FM and AFM ordering of the two M_S defects, i.e., $\Delta E_m = E^{AFM} - E^{FM}$, as a function of the distance d between the two M_S defects. (b) Relative positions of the two M_S defects considered in (a). With respect to the M_S defect denoted by the black circle, the first, second, third, and fourth nearest neighboring (NN) sites are represented by the blue, green, red, and pink circles, respectively.

have considered other large complex defects such as a W and two S vacancy complex and a six S vacancy cluster, which exhibit local magnetic moments. These results indicate that, although these complex defects could affect the magnetic properties of WS_2, the concentration of the large complex defects is so low, their effect could be insignificant even under non-equilibrium conditions. In this regard, we ignored the possible effect of large complex defects in the next section, and we focused on the long-range magnetic coupling between M_S defects, which are expected to be the most abundant magnetic defect in WS_2.

Until now, we have focused on the various defects in WS_2. We also studied the corresponding defects in MoS_2, for which the results are summarized in Table 1. Most of the results are qualitatively similar to those in WS_2. There is one thing to note: the formation energy of the Mo anti-site defect (Mo_S) is smaller than that of W_S in WS_2, so one can expect a higher Mo_S concentration. Thus, we believe that the qualitative magnetic properties induced by the native defects could be similar in both materials.

Table 2 Magnetic interaction ΔE_m and binding energy E_B of two anti-site defects M_S (M = W for WS_2 and Mo for MoS_2) with respect to the distance d between the two M_S defects. ΔE_m was calculated from the energy difference between the ferromagnetic E^{FM} and antiferromagnetic E^{AFM} orderings of the two defects, i.e., $\Delta E_m = E^{AFM} - E^{FM}$. E_B was measured from the energy gain of the two defects with respect to the isolated two defects

	WS_2			MoS_2		
	d (Å)	ΔE_m (meV)	E_B (eV)	d (Å)	ΔE_m (meV)	E_B (eV)
2 M_S-1NN	3.18	239	0.27	—	—	—
2 M_S-2NN$_{AC}$	5.51	−17	0.12	5.52	−2.0	0.06
2 M_S-2NN$_{ZZ}$	6.37	53	0.07	6.37	21	0.01
2 M_S−3NN$_{AC}$	8.42	1.4	0.04	8.43	1.4	0.03
2 M_S-3NN$_{ZZ}$	9.55	0.6	0.02	9.55	0.6	0.01
2 M_S-4NN	11.48	0.2	0.02	11.48	0.1	0.00

3.2. Long-range magnetic interaction of cation anti-site defects

To investigate the long-range ordering of the local magnetic moments in native defects and the defect-induced ferromagnetism in TMDs, the magnetic interaction between two M_S defects (M = W for WS_2 and Mo for MoS_2) was considered in a 7×7 supercell, in which the M_S concentration was 2% with respect to the total number of M atoms. This defect concentration is experimentally accessible in the TMDs.[35] As a measure of the magnetic interaction ΔE_m, we considered the energy differences between ferromagnetic (FM) and antiferromagnetic (AFM) ordering of the two M_S defects, i.e., $\Delta E_m = E^{AFM} - E^{FM}$, where E^{FM} and E^{AFM} are the total energy of the FM and AFM orderings. Fig. 3(a) shows ΔE_m as a function of the distance d between two M_S defects, and the results are also summarized in Table 2. Here, the positive (negative) ΔE_m indicates that the FM (AFM) ordering is stable.

We considered various relative positions between two M_S defects up to the fourth nearest neighboring (NN) site, and the positions are represented in Fig. 3(b); with respect to the M_S defect circled in black, the first, second, third, and fourth NN sites of the other M_S defects are designated by blue, green, red, and pink circles. We denote the two n-th NN M_S defects as 2M_S-nNN$_X$. If more than one n-th NN site exist, the different sites are distinguished using the subscript X, which can be ZZ or AC depending on whether the two defects are aligned along the zigzag or armchair direction, respectively [see Fig. 3(b)]. For 2W_S-1NN in WS_2, the two W_S atoms were relaxed away from the S atoms but relaxed inward between them, forming a bond between the two W atoms. This lowers the total energy of the two defects by 0.27 eV. Because the distance between the two defects is close enough for their spin densities to interact [see inset of Fig. 2(a)], the magnetic interaction ΔE_m is measured to be relatively large (239 meV), as shown in Fig. 3(a) and Table 2.

For 2W_S-2NN, there are two inequivalent positions: two W_S are separated along the armchair line (2W_S-2NN$_{AC}$) or zigzag
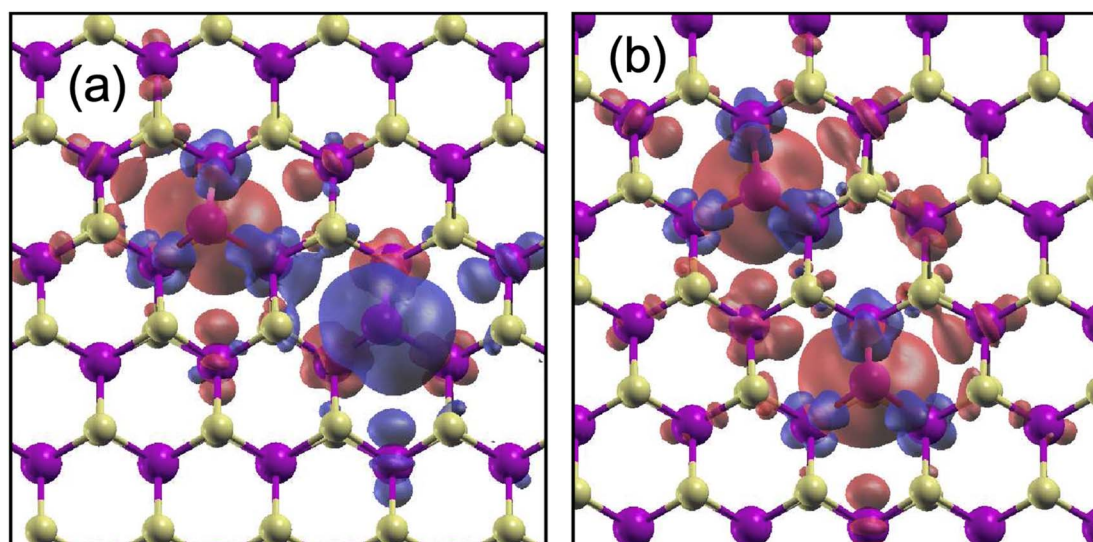

Fig. 4 Spin density for (a) 2W_S-2NN$_{AC}$ and (b) 2W_S-2NN$_{ZZ}$ in WS_2. Red (blue) contours represent the spatial distribution of the majority (minority) spin.

line (2W$_S$-2NN$_{ZZ}$) [see Fig. 3(b)]. The distance d between the two W$_S$ defects in 2W$_S$-2NN$_{AC}$ is shorter by 0.5 Å than that in 2W$_S$-2NN$_{ZZ}$. Among the relative positions that we have considered, only 2W$_S$-2NN$_{AC}$ prefers the AFM coupling by 17 meV compared to the FM coupling. The favorable AFM coupling reflects the spin density oscillation in W$_S$ [see inset of Fig. 2(a)]. As we mentioned above, if the majority spin is distributed on the W$_S$ atom, the minority spin is distributed on the NN W atoms, and again the majority spin is distributed on the next NN W atoms. Thus, because of the relative position of the two W$_S$ defects in 2W$_S$-2NN$_{AC}$, the spin distribution of the AFM coupling becomes compatible with the spin distribution of each W$_S$, as shown in Fig. 4(a). For 2W$_S$-2NN$_{ZZ}$, on the other hand, the spin distributions are compatible in the FM coupling [see Fig. 4(b)], and our results thus show that the energy of the FM coupling is lower by 53 meV than that of the AFM coupling.

The magnetic interaction is mediated by the spin density of each W$_S$ defect. Because the spin density is localized around W$_S$, as shown in the inset of Fig. 2(a), ΔE_m decreases with respect to d [see Table 2 and the inset of Fig. 3(a)]. However, a finite and positive ΔE_m (FM coupling) still exists for the third and fourth NN configurations, for which d is over 8 Å. The d-dependent magnetic interaction is also reflected in the splitting of the degenerate d$_{XY}$ and d$_{X^2-Y^2}$ levels within the band gap. Fig. 5 shows the total and projected DOSs of 2W$_S$-2NN$_{ZZ}$, 2W$_S$-3NN$_{AC}$, and 2W$_S$-3NN$_{ZZ}$. As shown in Fig. 5(a), each W$_S$ defect has occupied d$_{XY}$ and d$_{X^2-Y^2}$ levels and the empty d$_{Z2}$ level in the gap. For 2W$_S$-2NN$_{ZZ}$, the occupied d$_{XY}$ and d$_{X^2-Y^2}$ levels, which are degenerate for the isolated case, exhibit a sizable energy splitting of about 0.17 eV due to the interaction between the defect levels. The electronic structures of 2W$_S$-3NN$_{AC}$ and 2W$_S$-3NN$_{ZZ}$ [see Fig. 5(b) and (c)] are similar to that of 2W$_S$-2NN$_{ZZ}$, but the level splittings are reduced to 0.09 and 0.07 eV, respectively, as d increases.

The strength of the magnetic interaction ΔE_m is on the same order of magnitude as that of magnetic Mn dopants in TMDs, which have been considered as a source leading to ferromagnetism.[14] For several TMDs, the calculated ΔE_m of the two Mn dopants are about 130–200 meV for the 1NN configuration and 5–70 meV for the 2NN$_{ZZ}$ configuration, which are comparable with the ΔE_m of W$_S$ in WS$_2$, as shown in Table 2 and Fig. 3(a). In this regard, we expect that the W$_S$ defect can induce the ferromagnetism experimentally observed in undoped WS$_2$. However, as discussed above, ΔE_m becomes small over the defect distance d of 8 Å, so long-range ferromagnetic ordering could be possible in highly defective systems.

In addition, we considered the ΔE_m of the Mo$_S$ defects in MoS$_2$. The results are very similar to those of W$_S$ in WS$_2$, but there are two differences. First, the 2Mo$_S$-1NN configuration is unstable, and during the ionic relaxation, the two Mo$_S$ defects are relaxed inward each other, forming bonds. This relaxation quenches the magnetic moment in Mo$_S$. Second, the ΔE_m is slightly smaller than that of W$_S$ in WS$_2$. This difference may be caused by the small d-orbital radius of the Mo atoms. Thus, for the same defect density of M$_S$, MoS$_2$ is less likely to show ferromagnetism. However, as discussed above, the formation energy of Mo$_S$ is smaller than that of W$_S$ (see Table 1). As such, more abundant Mo$_S$ defects could lead to ferromagnetism in MoS$_2$.
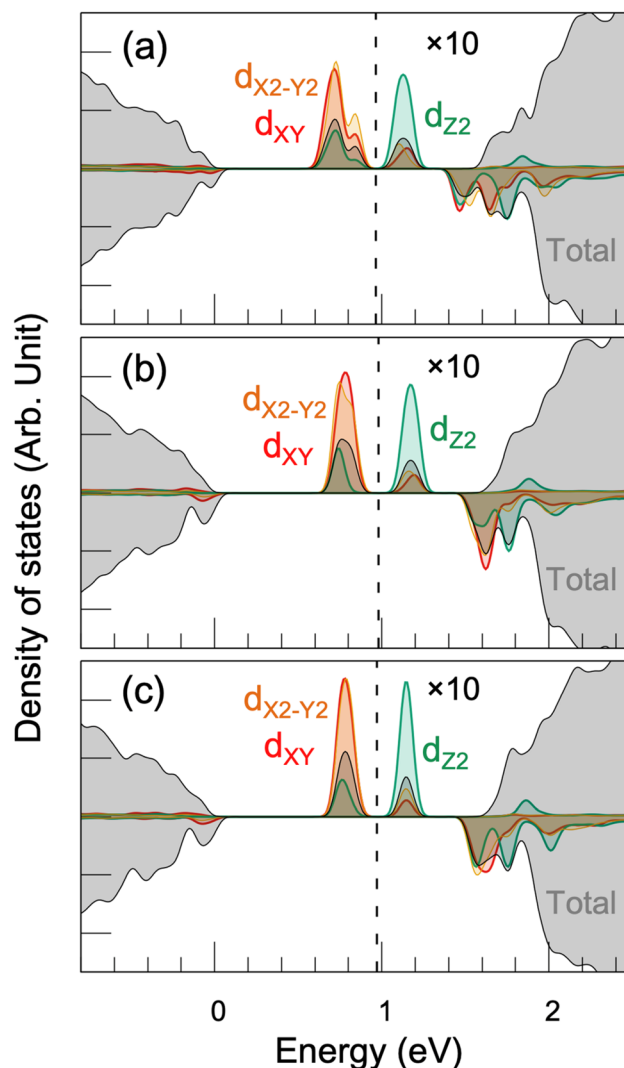

Fig. 5 Total and projected DOS for (a) 2W$_S$-2NN$_{ZZ}$, (b) 2W$_S$-3NN$_{AC}$, and (c) 2W$_S$-3NN$_{ZZ}$ in WS$_2$. Black lines and gray shaded regions are the total DOS, and projected DOS are shown using the corresponding colors denoted in the figures. All the projected DOSs were scaled by a factor of 10 with respect to the total DOS. Valence band maximum was set to 0.0 eV, and the Fermi level is presented by the vertical dotted lines.

4. Conclusions

In summary, we investigated various native defects in WS$_2$ and MoS$_2$ and found that the M$_S$ defect is the most abundant magnetic defect, exhibiting a local magnetic moment of $2\mu_B$, under non-equilibrium W-rich growth conditions. The spin density oscillation associated with the local magnetic moments mediates a long-range magnetic interaction between the M$_S$ defects, which mostly leads to ferromagnetic ordering. The strength of this magnetic interaction is comparable to that of magnetic dopants in TMDs. However, the interaction decreases significantly when the defect distance exceeds 9 Å. Thus, our findings suggest that ferromagnetism in TMDs can be induced in heavily defective TMD samples with a high concentration of M$_S$ defects.

Data availability

The data (the calculated atomic structures) supporting this article have been included as part of the ESI data.†

Conflicts of interest

There are no conflicts to declare.

Acknowledgements

References

1 B. Huang, *et.al.*, *Nature*, 2017, **546**, 270–273.
2 C. Gong, *et.al.*, *Nature*, 2017, **546**, 265–269.
3 N. D. Mermin and H. Wagner, *Phys. Rev. Lett.*, 1966, **17**, 1133.
4 M. Gibertini, M. Koperski, A. Morpurgo and K. S. Novoselov, *Nat. Nanotechnol.*, 2019, **14**, 408–419.
5 A. Soumyanarayanan, N. Reyren, A. Fert and C. Panagopoulos, *Nature*, 2016, **539**, 509–517.
6 A. Manchon, H. Koo, J. Nitta, S. Frolov and R. Duine, *Nat. Mater.*, 2015, **14**, 871–882.
7 D. Go, J.-P. Hanke, P. Buhl, F. Freimuth, G. Bihlmayer, H.-W. Lee, Y. Mokrousov and S. Blügel, *Sci. Rep.*, 2017, **7**, 46742.
8 X. Liu and M. Hersam, *Nat. Rev. Mater.*, 2019, **4**, 669–684.
9 B. Nikolić, K. Dolui, M. Petrović, P. Plecháč, T. Markussen and K. Stokbro, *First-Principles Quantum Transport Modeling of Spin-Transfer and Spin-Orbit Torques in Magnetic Multilayers*, Springer International Publishing, 2018.
10 G. Eda, H. Yamaguchi, D. Voiry, T. Fujita, M. Chen and M. Chhowalla, *Nano Lett.*, 2011, **11**, 5111–5116.
11 A. Durand, T. Clua-Provost, F. Fabre, P. Kumar, J. Li, J. H. Edgar, P. Udvarhelyi, A. Gali, X. Marie, C. Robert, J. M. Gérard, B. Gil, G. Cassabois and V. Jacques, *Phys. Rev. Lett.*, 2023, **131**, 116902.
12 K. S. Novoselov, A. K. Geim, S. V. Morozov, D. Jiang, Y. Zhang, S. V. Dubonos, I. V. Grigorieva and A. A. Firsov, *Science*, 2004, **306**, 666–669.
13 N. Mao, J. Tang, L. Xie, J. Wu, B. Han, J. Lin, S. Deng, W. Ji, H. Xu, K. Liu, L. Tong and J. Zhang, *J. Am. Chem. Soc.*, 2016, **138**, 300–305.
14 R. Mishra, W. Zhou, S. Pennycook, S. Pantelides and J.-C. Idrobo, *Phys. Rev. B: Condens. Matter Mater. Phys.*, 2013, **88**, 144409.
15 F. Zhang, *et.al.*, *Adv. Sci.*, 2020, **7**, 2001174.
16 D. Duong, S. Yun, Y. Kim, S.-G. Kim and Y. Lee, *Appl. Phys. Lett.*, 2019, **115**, 242406.
17 S. Fu, *et.al.*, *Nat. Commun.*, 2020, **11**, 2034.
18 A. K. Jena, S. K. Mallik, M. C. Sahu, S. Sahoo, A. K. Sahoo, N. K. Sharma, J. Mohanty, S. K. Gupta, R. Ahuja and S. Sahoo, *Sci. Rep.*, 2022, **12**, 2593.
19 A. Singh, C. C. Price and V. B. Shenoy, *ACS Nano*, 2022, **16**, 9452–9460.
20 Y. Sun, H. Zhang, Y. Zheng, P. Gao, C. Ye and F. Wang, *J. Alloys Compd.*, 2024, **994**, 174634.
21 O. V. Yazyev, *Phys. Rev. Lett.*, 2008, **101**, 037203.
22 O. V. Yazyev and L. Helm, *Phys. Rev. B: Condens. Matter Mater. Phys.*, 2007, **75**, 125408.
23 M. M. Ugeda, I. Brihuega, F. Guinea and J. M. Gómez-Rodríguez, *Phys. Rev. Lett.*, 2010, **104**, 096804.
24 J. J. Palacios, J. Fernández-Rossier and L. Brey, *Phys. Rev. B: Condens. Matter Mater. Phys.*, 2008, **77**, 195428.
25 H. Ohldag, P. Esquinazi, E. Arenholz, D. Spemann, M. Rothermel, A. Setzer and T. Butz, *New J. Phys.*, 2010, **12**, 123012.
26 H. Kim, J. Bang and J. Kang, *Sci. Rep.*, 2018, **8**, 13940.
27 H. González-Herrero, J. M. Gómez-Rodríguez, P. Mallet, M. Moaied, J. J. Palacios, C. Salgado, M. M. Ugeda, J.-Y. Veuillen, F. Yndurain and I. Brihuega, *Science*, 2016, **352**, 437–441.
28 O. V. Yazyev and M. I. Katsnelson, *Phys. Rev. Lett.*, 2008, **100**, 047209.
29 N. Huo, Y. Li, J. Kang, R. Li, Q. Xia and J. Li, *Appl. Phys. Lett.*, 2014, **104**, 202406.
30 R. Sanikop and C. Sudakar, *ACS Appl. Nano Mater.*, 2020, **3**, 576–587.
31 X. Ding, T. Liu, S. Ahmed, N. Bao, J. Ding and J. Yi, *J. Alloys Compd.*, 2019, **772**, 740–744.
32 L. Cai, J. He, Q. Liu, T. Yao, L. Chen, W. Yan, F. Hu, Y. Jiang, Y. Zhao, T. Hu, Z. Sun and S. Wei, *J. Am. Chem. Soc.*, 2015, **137**, 2622–2627.
33 X. Mao, Y. Xu, Q. Xue, W. Wang and D. Gao, *Nanoscale Res. Lett.*, 2013, **8**, 430.
34 S. Han, Y. Park, Y. Hwang, S. Jekal, M. Kang, W. Lee, W. Yang, G. D. Lee and S. Hong, *Sci. Rep.*, 2016, **6**, 38730.
35 J. Hong, *et.al.*, *Nat. Commun.*, 2015, **6**, 6293.
36 W. Zhou, X. Zou, S. Najmaei, Z. Liu, Y. Shi, J. Kong, J. Lou, P. Ajayan, B. Yakobson and J.-C. Idrobo, *Nano Lett.*, 2013, **13**, 2615–2622.
37 D. Yang, X. Fan, F. Zhang, Y. Hu and Z. Luo, *Nanoscale Res. Lett.*, 2019, **14**, 192.
38 P. Hohenberg and W. Kohn, *Phys. Rev.*, 1964, **136**, B864–B871.
39 W. Kohn and L. J. Sham, *Phys. Rev.*, 1965, **140**, A1133–A1138.
40 G. Kresse and J. Furthmüller, *Phys. Rev. B: Condens. Matter Mater. Phys.*, 1996, **54**, 11169–11186.
41 G. Kresse and J. Furthmüller, *Comput. Mater. Sci.*, 1996, **6**, 15–50.
42 G. Kresse and J. Hafner, *Phys. Rev. B: Condens. Matter Mater. Phys.*, 1994, **49**, 14251–14269.
43 G. Kresse and J. Hafner, *Phys. Rev. B: Condens. Matter Mater. Phys.*, 1993, **47**, 558–561.
44 P. E. Blöchl, *Phys. Rev. B: Condens. Matter Mater. Phys.*, 1994, **50**, 17953–17979.

45 J. P. Perdew, K. Burke and M. Ernzerhof, *Phys. Rev. Lett.*, 1997, **78**, 1396.

46 J. P. Perdew, K. Burke and M. Ernzerhof, *Phys. Rev. Lett.*, 1996, **77**, 3865–3868.

47 S. Steiner, K. Khmelevskyi, M. Marsmann and G. Kresse, *Phys. Rev. B*, 2016, **93**, 224425.

48 L. M. V. Ildefonso, E. L. Buthers, B. S. Archanjo, C. Legnani, W. G. Quirino, D. V. P. Massote, I. O. Maciel and B. Fragneaud, *J. Phys. Chem. C*, 2024, **128**, 7294–7305.

49 W.-F. Li, C. Fang and M. A. Van Huis, *Phys. Rev. B*, 2016, **94**, 195425.

50 J. Bang, Y.-S. Kim, C. Park, F. Gao and S. Zhang, *Appl. Phys. Lett.*, 2014, **104**, 252101.

51 C. Si, D. Choe, W. Xie, H. Wang, Z. Sun, J. Bang and S. Zhang, *Nano Lett.*, 2019, **19**, 3612–3617.

52 H.-P. Komsa and A. V. Krasheninnikov, *Phys. Rev. B: Condens. Matter Mater. Phys.*, 2015, **91**, 125304.

53 J. Chaste, J. Bang, I. Hnid, L. Khalil, C. Si, A. Durnez, X. Lafosse, M. Q. Zhao, A. T. Charlie Johnson, S. Zhang and A. Ouerghi, *ACS Nano*, 2020, **14**, 13611–13618.

54 X. Zhao, X. Dai, C. Xia and T. Wang, *Superlattices Microstruct.*, 2015, **85**, 339–347.

55 K. Momma and F. Izumi, *J. Appl. Crystallogr.*, 2011, **44**, 1272–1276.